nature materials

LETTERS

https://doi.org/10.1038/s41563-019-0585-z

Electronic structure of the parent compound of superconducting infinite-layer nickelates

M. Hepting[1,8], D. Li[1], C. J. Jia[1,*], H. Lu[1], E. Paris[2], Y. Tseng[2], X. Feng[1], M. Osada[1], E. Been[1], Y. Hikita[1], Y.-D. Chuang[3], Z. Hussain[3], K. J. Zhou[4], A. Nag[4], M. Garcia-Fernandez[4], M. Rossi[1], H. Y. Huang[5], D. J. Huang[5], Z. X. Shen[1,6], T. Schmitt[2], H. Y. Hwang[1], B. Moritz[1], J. Zaanen[7], T. P. Devereaux[1] and W. S. Lee[1,*]

The search continues for nickel oxide-based materials with electronic properties similar to cuprate high-temperature superconductors[1–10]. The recent discovery of superconductivity in the doped infinite-layer nickelate $NdNiO_2$ (refs. [11,12]) has strengthened these efforts. Here, we use X-ray spectroscopy and density functional theory to show that the electronic structure of $LaNiO_2$ and $NdNiO_2$, while similar to the cuprates, includes significant distinctions. Unlike cuprates, the rare-earth spacer layer in the infinite-layer nickelate supports a weakly interacting three-dimensional 5*d* metallic state, which hybridizes with a quasi-two-dimensional, strongly correlated state with $3d_{x^2-y^2}$ symmetry in the NiO_2 layers. Thus, the infinite-layer nickelate can be regarded as a sibling of the rare-earth intermetallics[13–15], which are well known for heavy fermion behaviour, where the NiO_2 correlated layers play an analogous role to the 4*f* states in rare-earth heavy fermion compounds. This Kondo- or Anderson-lattice-like 'oxide-intermetallic' replaces the Mott insulator as the reference state from which superconductivity emerges upon doping.

Although the mechanism of superconductivity in cuprates remains a subject of intense research, early on it was suggested that the conditions required for realizing high-temperature superconductivity are rooted in the physics of a two-dimensional (2D) electron system subject to strong local repulsion[16,17]. This describes Mott (charge-transfer) insulators in the stoichiometric parent compounds, characterized by spin-½ Heisenberg antiferromagnetism, from which superconductivity emerges upon doping. A long-standing question exists as to whether these 'cuprate–Mott' conditions can be realized in other oxides, and extensive efforts to synthesize and engineer nickel oxides (nickelates) promised such a realization[1–10]. Infinite-layer $NdNiO_2$ became the first such nickelate superconductor following the recent discovery of superconductivity in Sr-doped samples[11]. The undoped parent compound, produced by removing the apical oxygen atoms from the perovskite nickelate $NdNiO_3$ using a metal hydride-based soft chemistry reduction process[10,18–20], appears to be a close sibling of the cuprates—it is isostructural to the infinite-layer cuprates with monovalent Ni^{1+} cations and possesses the same $3d^9$ electron count as Cu^{2+} cations in undoped cuprates. Yet, as we will reveal, the electronic structure of the undoped $RNiO_2$ (R = La and Nd) remains distinct from the Mott, or charge-transfer, compounds of undoped cuprates and even other nickelates.

As a reference, we first discuss the electronic structure of the canonical nickelates, NiO and $LaNiO_3$. The rocksalt NiO is a charge-transfer insulator, as characterized in the Zaanen–Sawatzky–Allen scheme[21], whose charge-transfer energy Δ (promoting charge from oxygen ligands to Ni *d* orbitals) lies below the Coulomb interaction scale U on Ni sites. The valence Ni *d* orbitals strongly hybridize with oxygen ligands, yielding wavefunctions with mixed character $\alpha|3d^8\rangle+\beta|3d^9\underline{L}\rangle$ ($\alpha^2+\beta^2=1$), with $\beta^2\approx0.2$ (refs. [22,23]) per NiO_6 octahedron, where $\underline{L}$ denotes a ligand hole on the oxygens. Such Ni–O ligand hybridization gives rise to a pre-peak in X-ray absorption spectroscopy (XAS) near the O K-edge (Fig. 1a). In addition, a large bandgap set by Δ appears in the oxygen partial density of states (PDOS) obtained both experimentally (Fig. 1b) and from density functional theory with on-site Coulomb interaction potential (LDA+U) calculations (Fig. 1e). In the perovskite $RNiO_3$, where formal valence counting would give Ni^{3+} ($3d^7$), both theoretical and experimental studies indicate that the perovskite structure leads to a decrease of Δ, such that it effectively becomes negative[24]. Under such a scenario, electrons from oxygen ligands spontaneously transfer to Ni cations, giving rise to 'self-doped' holes on the ligands, and a pre-peak in the O K-edge XAS (Fig. 1a). As expected for a negative charge-transfer metal, no bandgap appears in the oxygen PDOS (Fig. 1c,f)[25].

The O K-edge XAS tells a very different story for the infinite-layer nickelates $LaNiO_2$ and $NdNiO_2$, as shown in Fig. 1a. The lack of a pre-edge peak suggests that the oxygen ligands carry significantly less weight in the ground-state wavefunction, signalling a weaker effective mixing between oxygen and the Ni^+ cations. Unlike NiO and $LaNiO_3$, the oxygen PDOS (Fig. 1d) exhibits a diminished weight near the Fermi energy, especially in the unoccupied states, also indicating that O 2*p* orbitals carry less weight in the expected upper Hubbard band by comparison, all of which is consistent with the calculated oxygen PDOS from LDA + U (Fig. 1g).

Although the oxygen electronic structure deviates significantly from other nickelates and cuprates[26], we examined the electronic structure of the Ni cation in $RNiO_2$ using both XAS and resonant inelastic X-ray scattering (RIXS) at the Ni L_3-edge (a core-level 2*p* to valence 3*d* transition). As shown in Fig. 2a, while XAS spectra for

---

[1] Stanford Institute for Materials and Energy Sciences, SLAC National Accelerator Laboratory, Menlo Park, CA, USA. [2] Photon Science Division, Swiss Light Source, Paul Scherrer Institut, Villigen, Switzerland. [3] Advanced Light Source, Lawrence Berkeley National Laboratory, Berkeley, CA, USA. [4] Diamond Light Source, Harwell Science and Innovation Campus, Didcot, UK. [5] NSRRC, Hsinchu Science Park, Hsinchu, Taiwan. [6] Geballe Laboratory for Advanced Materials, Departments of Physics and Applied Physics, Stanford University, Stanford, CA, USA. [7] Instituut-Lorentz for theoretical Physics, Leiden University, Leiden, the Netherlands. [8] Present address: Max Planck Institute for Solid State Research, Stuttgart, Germany.
*e-mail: chunjing@stanford.edu; leews@stanford.edu

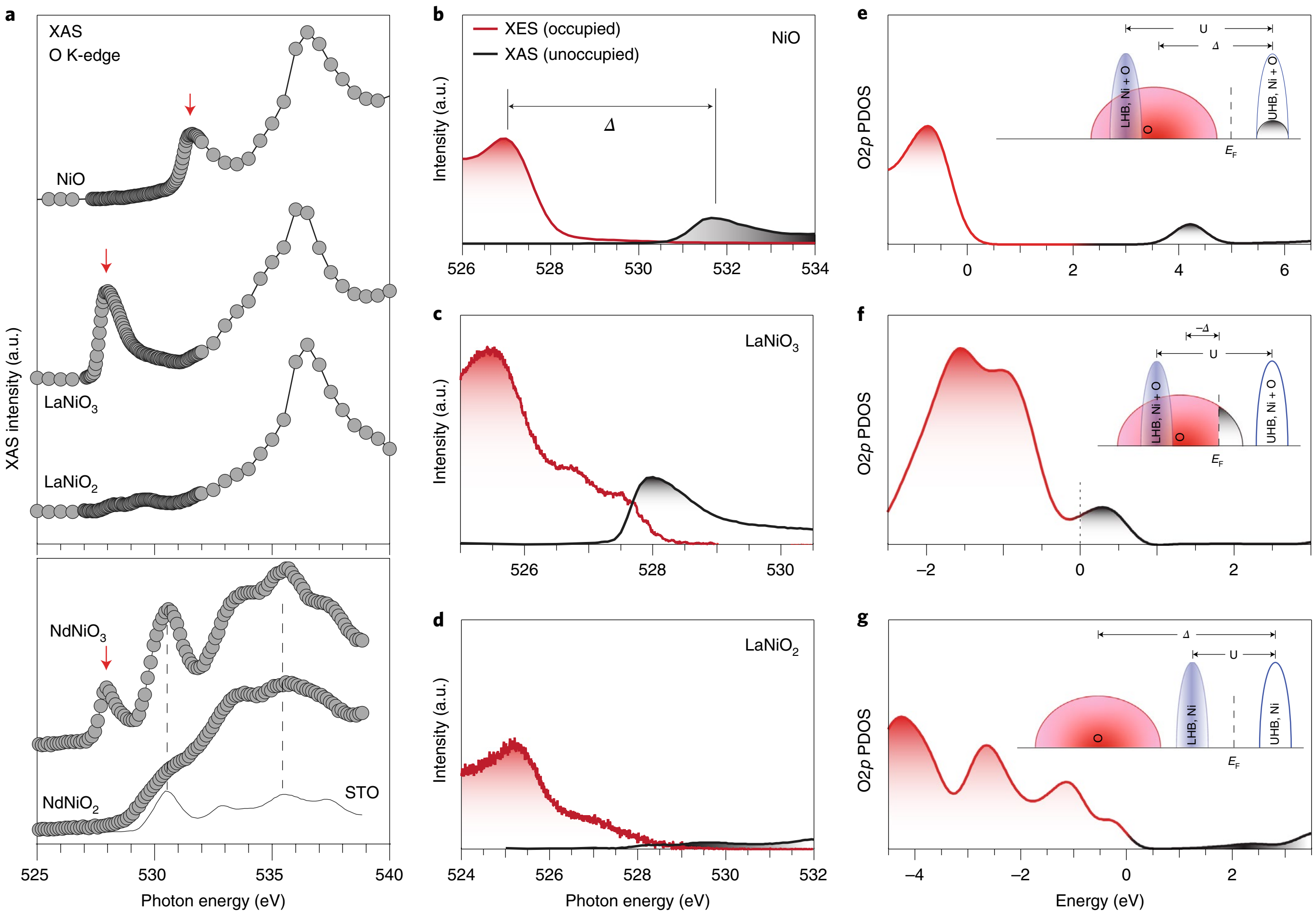

Fig. 1 | X-ray spectroscopy near the O K-edge and LDA + *U* calculation. a, Upper panel: XAS spectra for NiO, LaNiO$_3$ and LaNiO$_2$. Red arrows mark the pre-edge peaks indicative of Ni-O hybridization. The lower panel shows the XAS of NdNiO$_3$ and NdNiO$_2$. Dashed vertical lines indicate features of the SrTiO$_3$ (STO) substrate (solid grey line) in the XAS spectra of NdNiO$_3$ and NdNiO$_2$ due to the film thickness being thinner than that of the La-based films shown in the upper panel. Spectra are vertically offset for clarity. **b–d**, X-ray emission spectra (XES) and XAS in the pre-edge region, roughly reflecting the occupied (red shading) and unoccupied (black shading) oxygen PDOS, respectively. Vertical lines illustrate the bandgap projected in the oxygen DOS, corresponding to the effective charge-transfer energy *Δ* in NiO and LaNiO$_3$. **e–g**, LDA + *U* calculations for the PDOS with O 2*p* orbital character ($U = 8$ eV for NiO and LaNiO$_3$, $U = 6$ eV for LaNiO$_2$). Red and black shading indicates the occupied and unoccupied oxygen PDOS, respectively. Insets: sketches of the relationship between *U* and *Δ* in the Zaanen–Sawatzky–Allen scheme for each compound. UHB and LHB stand for upper and lower Hubbard band, respectively.

both NiO and LaNiO$_3$ exhibit distinct multi-peak structures originating from $2p^63d^8$–$2p^53d^9$ and $2p^63d^8L^n$–$2p^53d^9L^n$ multiplet transitions, respectively[23,24], XAS for the infinite-layer nickelates shows a main absorption peak (denoted A) that closely resembles the single peak associated with the $2p^63d^9$–$2p^53d^{10}$ transition in cuprates[27]. In particular for LaNiO$_2$, the XAS exhibits an additional lower-energy shoulder A′. In the RIXS map shown in Fig. 2b, the ~1 and ~1.8 eV features resemble the *dd* excitations seen in LaNiO$_3$ (Fig. 2c) and NdNiO$_3$ (ref. [24]), except they are broader and exhibit a dispersion with incident photon energy. This suggests that the Ni 3*d* states in LaNiO$_2$ are mixed with delocalized states, probably the La^{3+} 5*d* states. Interestingly, at the A′ resonance, a 0.6 eV feature appears that is absent in the RNiO$_3$ compounds (Fig. 2c,e and ref. [24]). Using exact diagonalization (see Methods), we reproduce the general features from XAS and RIXS (Fig. 2f–h), including the A′ features, highlighting the hybridization between the Ni $3d_{x^2-y^2}$ and La 5*d* orbitals. Thus, in configuration interaction, the Ni state can be expressed as a combination of $|3d^9\rangle$ and $|3d^8R\rangle$, where *R* denotes a charge-transfer to the rare-earth cation (see Methods and Supplementary Table 2). RIXS measurements across the La M$_4$-edge (3*d*–4*f* transition) do not show any signatures of 4*f* orbital excitations, as expected for the completely empty 4*f* shell of the La^{3+} cation (Extended Data Fig. 3). Hence, we argue that the La 4*f* states are frozen in the core and not hybridized with Ni 3*d* states (Extended Data Fig. 2). In NdNiO$_2$, the ~0.6 eV feature due to the Nd–Ni hybridization also exists in RIXS (Fig. 2d,e), but its resonance energy (A′) almost coincides with the main absorption peak A. As a consequence, the A′ feature cannot be resolved in XAS (Fig. 2a). We note that the separation between A and A′ depends on the energetic balance among microscopic parameters, including site energy, charge-transfer energy and rare-earth Ni hybridization energy, which are expected to vary between infinite-layer nickelates as a function of the rare-earth element.

To further analyse the electronic structure, we turn to density functional theory (DFT). The LDA + *U* scheme[28] has a long track record of correctly reproducing the gross features of correlated electronic structure for transition metal oxides. Although generally first principle, one cannot be certain about the value of the local Coulomb interaction *U*; however, we can put bounds on it. The infinite-layer nickelates are undoubtedly less good metals than elemental nickel, characterized by $U \approx 3$ eV, which we can take as a lower bound. From O K-edge XAS, the Coulomb interaction should be smaller than that of the large-bandgap charge-transfer insulator NiO, where

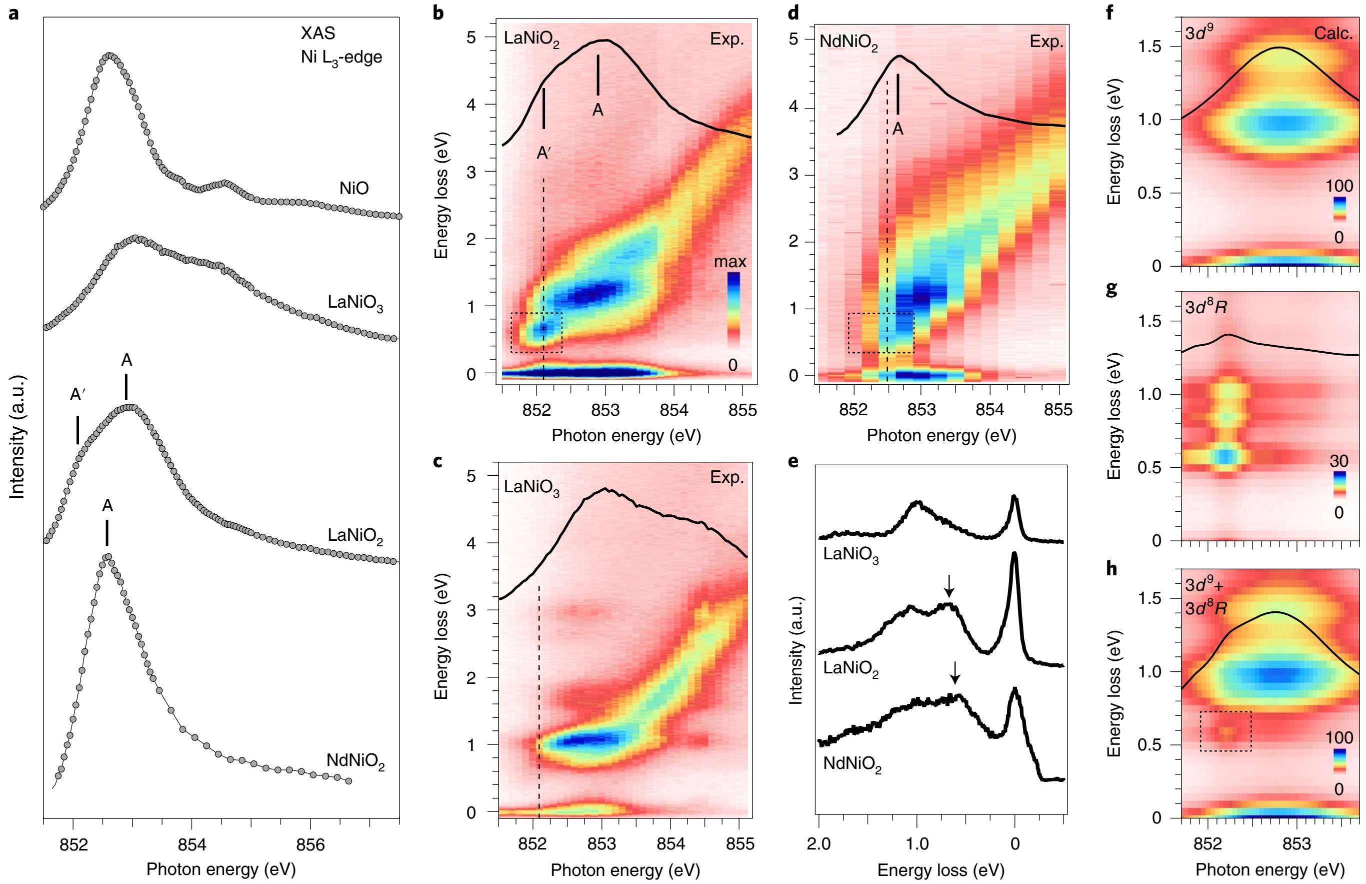

Fig. 2 | XAS and RIXS at the Ni L_3-edge. a, XAS of NiO, $LaNiO_3$, $LaNiO_2$ and $NdNiO_2$. The La M_4-line was subtracted from the $LaNiO_2$ and $LaNiO_3$ spectra (Extended Data Fig. 2). The markers A indicate the main peak of $LaNiO_2$ and $NdNiO_2$. A′ labels a lower-energy shoulder in the XAS of $LaNiO_2$. Spectra are vertically offset for clarity. **b**–**d**, RIXS intensity map of $LaNiO_2$, $LaNiO_3$ and $NdNiO_2$ measured as a function of incident photon energy at $T=20$ K. The corresponding XAS are superimposed as a solid black line in each map. The dashed boxes in **b** and **d** highlight the ~0.6 eV features of $LaNiO_2$ and $NdNiO_3$ that are associated with the Ni–La and Ni–Nd hybridizations, respectively. **e**, RIXS energy loss spectra of $LaNiO_3$, $LaNiO_2$ and $NdNiO_2$ at incident energies indicated by vertical dashed lines in **b**–**d**. Black arrows highlight the 0.6 eV features of $LaNiO_2$ and $NdNiO_2$. **f**–**h**, Calculated RIXS maps and absorption spectra (solid black lines) of $LaNiO_2$ for $3d^9$ (**f**), $3d^8R$ (**g**) and $3d^9+3d^8R$ (**h**) (R denotes a charge-transfer to the rare-earth cation) ground state, respectively. The dashed box in **h** highlights the same feature as the box in **b**.

$U\approx8$ eV. Here, we choose $U=6$ eV in our calculations for $LaNiO_2$ (with a lowest energy antiferromagnetic solution, see Methods for details), revealing some salient features that correlate with experimental observations. (1) As shown in Fig. 1g (and Fig. 3a), when compared to other nickelates, the oxygen 2p bands lie significantly further away from the Fermi energy, signalling reduced oxidation and implying a charge-transfer energy Δ that exceeds U. This places the $RNiO_2$ infinite-layer nickelates within the Mott–Hubbard regime of the Zaanen–Sawatzky–Allen scheme[21]. (2) The density of states near E_F is dominated by the half-filled Ni $3d_{x^2-y^2}$ states, which appear isolated from the occupied Ni 3d bands. The characteristic lower and upper Hubbard bands (Fig. 3a), at least in part, signal a textbook single-band Hubbard model, all but confirming that the Ni cation should be in a very nearly monovalent $3d^9$ state, consistent with the Ni L-edge XAS and RIXS (Fig. 2). (3) The density of states at E_F is actually finite, but small, as shown upon closer inspection of Fig. 3a,b. Near the Γ point, a Fermi surface pocket forms that is mainly of La 5d character (Fig. 3b); it is quite extended and 3D (see the wavefunction at a Fermi momentum k_F, Fig. 3c, and the Fermi surface, Fig. 3d). This contrasts with the 2D nature of the correlated $3d_{x^2-y^2}$ Ni states (Fig. 3b). In other words, the electronic structure of the infinite-layer nickelate consists of a low-density 3D metallic rare-earth band coupled to a 2D Mott system.

To theoretically investigate emergent phenomena in infinite-layer nickelates, a low-energy effective model can be derived as a starting point. A minimal model for these materials would look like

$$H=\sum_{k,\sigma}\left(\varepsilon_k^{\rm R}n_{k,\sigma}^{\rm R}+\varepsilon_k^{\rm Ni}n_{k,\sigma}^{\rm Ni}\right)+U\sum_i n_{i,\uparrow}^{\rm Ni}n_{i,\downarrow}^{\rm Ni}+\sum_{k,i,\sigma}\left(V_{k,i}c_{k,\sigma}^{\dagger}d_{i,\sigma}+{\rm h.c.}\right)$$

where the first term describes the non-interacting rare-earth (R) and Ni bands with energies $\varepsilon_k^{\rm R}$ and $\varepsilon_k^{\rm Ni}$, respectively, the second term represents the usual on-site Hubbard interaction with strength U in the quasi-two-dimensional Ni layer, and the third term describes the coupling with strength $V_{k,i}$ between the R and Ni subsystems. Here, $n_{k,\sigma}^{\rm R}$ and $n_{k,\sigma}^{\rm Ni}$ represent the usual number operators for the R and Ni subsystems, while $c_{k,\sigma}^{\dagger}$ ($c_{k,\sigma}$) and $d_{k,\sigma}^{\dagger}$ ($d_{k,\sigma}$) create (annihilate) electrons in the 3D metallic R and 2D Hubbard-like Ni subsystems, respectively. This model resembles the Anderson-lattice (or Kondo-lattice) model for the rare-earth intermetallics[13–15], but with the notable addition of a weakly hybridized single-band Hubbard-like model for the Ni layer, rather than strongly interacting 4f states

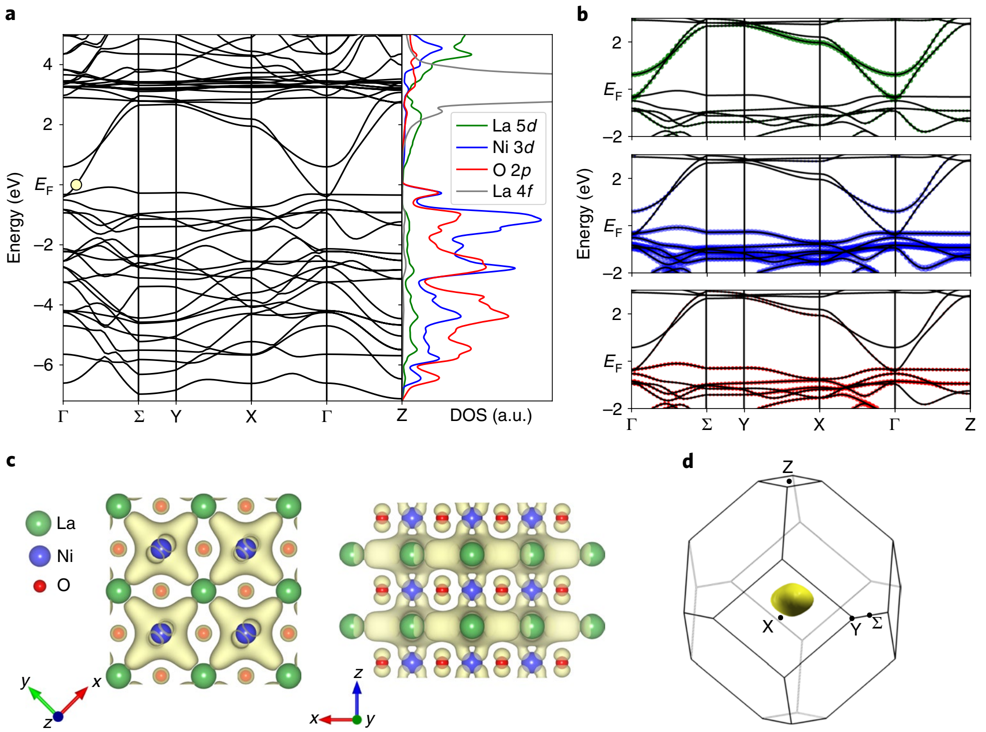

Fig. 3 | Electronic structure of LaNiO$_2$. Theoretical calculations of the electronic structure in the LDA + U framework with U = 6 eV (antiferromagnetic solution). **a**, Band structure of LaNiO$_2$ along high symmetry directions in the body centred tetragonal (bct) Brillouin zone. The Brillouin zone with labelled high symmetry points is also shown in **d**. The right-hand side shows the La 5*d* (green), Ni 3*d* (blue), O 2*p* (red) and La 4*f* (grey) PDOS with a smaller energy broadening than that used in Fig. 1e–g. **b**, Orbital projected band structure of LaNiO$_2$ near E_F. The colour code is identical to that used in **a**, representing the projection onto orbitals with different atomic character. **c**, Top and side views of an electron density contour for the single-particle wavefunction at Fermi momentum k_F along Γ–Σ (yellow marker in **a**). **d**, Fermi surface (closed electron pocket) around Γ with dominant La 5*d* character in the first bct Brillouin zone with labelled high symmetry points.

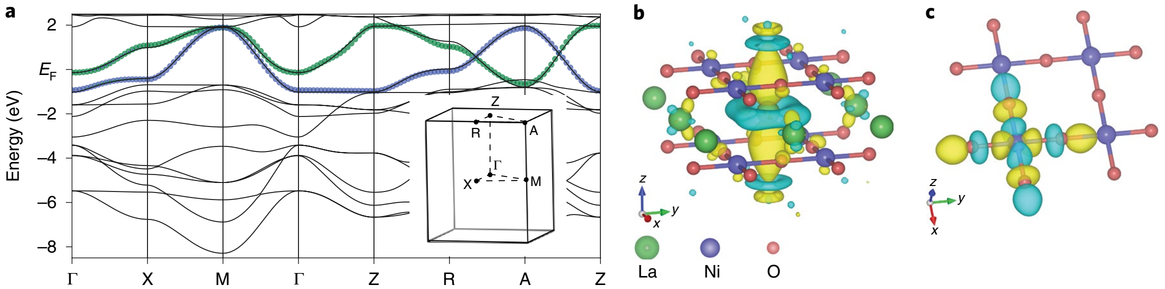

Fig. 4 | Deriving a minimal model for the rare-earth infinite-layer nickelates. a, Band dispersion of LaNiO$_2$, highlighting two bands that cross E_F in the paramagnetic LDA calculation. The inset shows the high symmetry points in the tetragonal Brillouin zone. **b**,**c**, Isosurface plots for an extended La-centred $d_{3z^2-r^2}$-like (**b**) and essentially planar Ni-centred $d_{x^2-y^2}$-like (**c**) Wannier orbital for the minimal low-energy model of LaNiO$_2$. These two orbitals produce the 3D band (La, green) and quasi-2D band (Ni, blue) highlighted in **a**. The derived parameters of the minimal model are listed in Supplementary Table 3.

(or localized spin moments). We can take this a step further and derive the parameter of this model Hamiltonian by performing Wannier 'downfolding' on the band structure in the one-Ni unit cell with U = 0 eV. Figure 4a shows the band structure for LaNiO$_2$ obtained from LDA without a Hubbard U (see Supplementary Information for details). Here, consistent with previous calculations[2], two bands cross the Fermi level: a fully 3D band with predominantly La 5*d* character and a quasi-2D band with Ni 3*d* character. Wannier downfolding[29] produces one extended orbital with $d_{3z^2-r^2}$ symmetry centred on La (Fig. 4b) and another orbital confined primarily to the NiO$_2$ planes with $d_{x^2-y^2}$ symmetry centred on Ni (Fig. 4c), which are fully consistent with the expected orbital arrangements given the crystal and ligand field symmetries for this material and the LDA + U results shown in Fig. 3. Full details about the downfolded model, including effective model parameters, are provided in Supplementary Table 3.

This downfolded model is, to the best of our knowledge, unique to this particular system. Viewed theoretically, this 'Hubbard–Kondo' model is uncharted territory and it is a natural question to ask what happens to the basic single-band Hubbard model when its states weakly hybridize with a metallic band. For example, do the spins in the NiO$_2$ layers order antiferromagnetically or will the Kondo effect strongly screen the local moments and give rise to electronic band hybridizations[13–15] in analogy to the case of heavy fermions? Note that, unlike the rare-earth intermetallics, here Ni spins interact via the strong short-range super-exchange interaction, which replaces the Ruderman–Kittel–Kasuya–Yosida interactions in the heavy fermion compounds. More importantly, can superconductivity emerge in this model by introducing doped charge carriers? Apparently, experimental information, particularly about the Fermi surface and magnetic susceptibility, and information about other elementary excitations such as spin, charge and phonon excitations will be required to gain further insights. Nevertheless, our results have provided a glimpse into the remarkable electronic structure of the parent compounds of superconducting infinite-layer nickelates, which appear to serve as a birthplace of superconductivity upon doping.

Online content

Any methods, additional references, Nature Research reporting summaries, source data, extended data, supplementary information, acknowledgements, peer review information; details of author contributions and competing interests; and statements of data and code availability are available at https://doi.org/10.1038/s41563-019-0585-z.

Received: 5 September 2019; Accepted: 11 December 2019;
Published online: 20 January 2020

References

1. Anisimov, V. I., Bukhvalov, D. & Rice, T. M. Electronic structure of possible nickelate analogs to the cuprates. *Phys. Rev. B* **59**, 7901–7906 (1999).
2. Lee, K.-W. & Pickett, W. E. Infinite-layer $LaNiO_2$: Ni^{1+} is not Cu^{2+}. *Phys. Rev. B* **70**, 165109 (2004).
3. Botana, A. S., Pardo, V. & Norman, M. R. Electron doped layered nickelates: spanning the phase diagram of the cuprates. *Phys. Rev. Mater.* **1**, 021801(R) (2017).
4. Chaloupka, J. & Khaliullin, G. Orbital order and possible superconductivity in $LaNiO_3/LaMO_3$ superlattices. *Phys. Rev. Lett.* **100**, 016404 (2008).
5. Hansmann, P. et al. Turning a nickelate Fermi surface into a cuprate-like one through heterostructuring. *Phys. Rev. Lett.* **103**, 016401 (2009).
6. Middey, S. et al. Physics of ultrathin films and heterostructures of rare-earth nickelates. *Annu. Rev. Mater. Res.* **46**, 305–334 (2016).
7. Boris, A. V. et al. Dimensionality control of electronic phase transitions in nickel-oxide superlattices. *Science* **332**, 937–940 (2011).
8. Benckiser, E. et al. Orbital reflectometry of oxide heterostructures. *Nat. Mater.* **10**, 189–193 (2011).
9. Disa, A. S. et al. Orbital engineering in symmetry-breaking polar heterostructures. *Phys. Rev. Lett.* **114**, 026801 (2015).
10. Zhang, J. et al. Large orbital polarization in a metallic square-planar nickelate. *Nat. Phys.* **13**, 864–869 (2017).
11. Li, D. et al. Superconductivity in an infinite-layer nickelate. *Nature* **572**, 624–627 (2019).
12. Sawatzky, G. A. Superconductivity seen in a nickel oxide. *Nature* **572**, 592–593 (2019).
13. Fisk, Z., Ott, H. R., Rice, T. M. & Smith, J. L. Heavy-electron metals. *Nature* **320**, 124–129 (1986).
14. Coles, B. R. Heavy-fermion intermetallic compounds. *Contemp. Phys.* **28**, 143–157 (1987).
15. Stewart, G. R. Non-Fermi-liquid behavior in *d*- and *f*-electron metals. *Rev. Mod. Phys.* **73**, 797–855 (2001).
16. Mott, N. F. & Peierls, R. Discussion of the paper by de Boerand Verwey. *Proc. Phys. Soc.* **49**, 72–73 (1937).
17. Lee, P. A., Nagaosa, N. & Wen, X.-G. Doping a Mott insulator: physics of high-temperature superconductivity. *Rev. Mod. Phys.* **78**, 17–85 (2006).
18. Crespin, M. O., Isnard, O., F. Dubois, F., Choisnet, J. & Odier, P. $LaNiO_2$: synthesis and structural characterization. *J. Solid State Chem.* **178**, 1326–1334 (2005).
19. Hayward, M. A., Green, M. A., Rosseinsky, M. J. & Sloan, J. Sodium hydride as a powerful reducing agent for topotactic oxide deintercalation: synthesis and characterization of the nickel(i) oxide $LaNiO_2$. *J. Am. Chem. Soc.* **121**, 8843–8854 (1999).
20. Ikeda, A., Krockenberger, Y., Irie, H., Naito, M. & Yamamoto, H. Direct observation of infinite NiO_2 planes in $LaNiO_2$ films. *Appl. Phys. Express* **9**, 061101 (2016).
21. Zaanen, J., Sawatzky, G. A. & Allen, J. W. Band gaps and electronic structure of transition-metal compounds. *Phys. Rev. Lett.* **55**, 418 (1985).
22. Kuiper, P., Kruizinga, G., Ghijsen, J. & Sawatzky, G. A. Character of holes in $Li_xNi_{1-x}O$ and their magnetic behavior. *Phys. Rev. Lett.* **62**, 221 (1989).
23. Kurmaev, E. Z. et al. Oxygen X-ray emission and absorption spectra as a probe of the electronic structure of strongly correlated oxides. *Phys. Rev. B* **77**, 165127 (2008).
24. Bisogni, V. et al. Ground-state oxygen holes and the metal–insulator transition in the negative charge-transfer rare-earth nickelates. *Nat. Commun.* **7**, 13017 (2016).
25. Zaanen, J. & Sawatzky, G. A. Systematics in band gaps and optical spectra of 3D transition metal compounds. *J. Solid State Chem.* **88**, 8–27 (1990).
26. Chen, C. T. et al. Electronic states in $La_{2-x}Sr_xCuO_{4+\delta}$ probed by soft-X-ray absorption. *Phys. Rev. Lett.* **66**, 104 (1991).
27. Grioni, M. et al. Studies of copper valence states with Cu L_3 X-ray-absorption spectroscopy. *Phys. Rev. B* **39**, 1541 (1989).
28. Anisimov, V. I., Zaanen, J. & Anderson, O. K. Band theory and Mott insulators: Hubbard *U* instead of Stoner *I*. *Phys. Rev. B* **44**, 943 (1991).
29. Haverkort, M. W., Zwierzycki, M. & Andersen, O. K. Multiplet ligand-field theory using Wannier orbitals. *Phys. Rev. B* **85**, 165113 (2012).

Methods

Materials. $LaNiO_3$ films with 12 and 50 nm thicknesses were grown on top of $5\times5\,mm^2$ TiO_2-terminated $SrTiO_3$ (001) substrates by pulsed laser deposition using a 248 nm KrF excimer laser. Before growth, $SrTiO_3$ substrates were pre-annealed at an oxygen partial pressure (p_{O_2}) of 5×10^{-6} torr for 30 min at 950 °C to achieve sharp step-and-terrace surfaces. The films were subsequently grown at a substrate temperature T_g of 575 °C and $p_{O_2}=34$ mtorr, using $1.4\,J\,cm^{-2}$ laser fluence and $4\,mm^2$ laser spot size on the target. The growth was monitored by reflection high-energy electron diffraction intensity oscillations. After the growth, the samples were cooled to room temperature in the same oxygen environment. Characterization by X-ray diffraction (XRD) scans with Cu Kα radiation indicated the presence of the perovskite phase of (001)-oriented $LaNiO_3$ and high epitaxial quality for all as-grown films. AFM topographic scans showed atomically flat surfaces. Reducing conditions[30] were adapted to remove apical oxygen to produce both the (001)-oriented $LaNiO_{2.5}$ and $LaNiO_2$ phases. For reduction experiments, each $LaNiO_3$ sample was cut into two pieces with dimensions of $2.5\times5\,mm^2$. The $2.5\times5\,mm^2$ sample was then vacuum-sealed together with blocks of CaH_2 powder in a Pyrex glass tube (pressure <0.1 mtorr). The tube was heated to 240 °C at a rate of $10\,°C\,min^{-1}$ and kept at this temperature for 30–120 min, before being cooled to room temperature at a rate of $10\,°C\,min^{-1}$. After the annealing process, remnant CaH_2 powder on the sample surface was rinsed off with 2-butanone. The XRD scans in Extended Data Fig. 1a show the characteristic Bragg peaks of the 12 nm $LaNiO_3$ film and the ~50 nm $LaNiO_2$ film used in the XAS and RIXS measurements in the main text. Additionally, a ~50 nm $LaNiO_{2.5}$ film was characterized as a reference sample. The 2θ peak positions of these three films coincide with that of similar films on $SrTiO_3$ (ref. [30]). The c-axis lattice constants extracted from the XRD scans were 3.809, 3.771 and 3.407 Å for the $LaNiO_3$, $LaNiO_{2.5}$ and $LaNiO_2$ films, respectively. In comparison to $LaNiO_2$ powder[17,30], the c-axis lattice constant of the film is slightly expanded due to the compressive strain induced by the $SrTiO_3$ substrate.

$NdNiO_2$ films grown on a $SrTiO_3$ substrate with a thickness of ~10 nm were prepared using the conditions described in ref. [11]. $NdNiO_2$ films with and without a capping layer of 5 unit cells of $SrTiO_3$ were measured and show the same spectral properties. As a reference, we also measured a $NdNiO_3$ film grown on a $SrTiO_3$ substrate and capped with 5 unit cells of $SrTiO_3$.

Extended Data Fig. 1b displays the resistivity as a function of temperature of the $LaNiO_3$ film in a four-probe geometry, which shows metallic behaviour down to 2 K. The $LaNiO_2$ film exhibits higher resistivity than $LaNiO_3$ at 300 K, which increases further with decreasing temperature (Extended Data Fig. 1b). Similar transport properties are reported in refs. [20,30,31].

Commercially available NiO powder (≥99.995% purity, Sigma-Aldrich) was used for the measurements.

XAS and RIXS measurements. The XAS and RIXS spectra of the La-based nickelate samples were measured at the ADRESS beamline with the SAXES spectrometer at the Swiss Light Source (SLS) of the Paul Scherrer Institut[32]. For RIXS measurements the scattering angle was fixed to 130° and the combined instrument resolution was ~100 meV at the Ni L_3-edge. The scattering plane coincided with the crystallographic a–c (b–c) plane with a grazing incident angle of $\theta=15°$. The XES and RIXS spectra shown in Fig. 1 were measured with π-polarized incident photons. Due to the strong fluorescence signal from the STO substrate, the XES of $LaNiO_3$ and $LaNiO_2$ shown in Fig. 1 were obtained from the fluorescence signal identified in RIXS incident-photon-energy and emission-energy map across the oxygen pre-edge (incident photon energy from ~525 eV to ~530 eV). The elastic line and weak Raman-like excitations (in $LaNiO_2$) were removed for clarity.

The XAS and XES spectra of NiO shown in Fig. 1a were measured at beamline BL8.0 using the q-RIXS endstation of the Advanced Light Source (ALS) of the Lawrence Berkeley National Laboratory. For the RIXS/XES measurements the scattering angle was fixed at 130° and the combined instrument resolution was ~300 meV at the Ni L_3-edge and ~200 meV at the O K-edge. The XAS spectra at the O K-edge for $NdNiO_3$ and $NdNiO_2$ (Fig. 1a) were taken at 41A BlueMagpie beamline at Taiwan Photon Source. The XAS and RIXS maps at the Ni L-edge of $NdNiO_2$ were taken at beamline I21 at the Diamond Light Source. The RIXS spectrometer was set at 146°, with a resolution of ~50 meV. The scattering plane coincided with the crystallographic a–c (b–c) plane with a grazing incident angle of ~10°. π-polarized incident photons were used for this measurement.

All XAS spectra at the O K-edge (Fig. 1) were taken in fluorescence yield mode with a grazing incident angle of 10 and 20° for the La-based and Nd-based nickelates, respectively. The grazing incident geometry was used to reduce the signal arising from the STO substrate. The spectra were normalized such that the intensity at the pre-edge and the post-edge were 0 and 1, respectively.

All XAS spectra at the Ni L-edge (Fig. 2) were taken in fluorescence yield mode with normal incident geometry. These XAS were normalized such that the intensity at the pre-edge and the post-edge were 0 and 1, respectively. For the XAS spectra for the La-based nickelates, the intense La M_4-line centred around 850.5 eV (Extended Data Fig. 2a) was fitted by a Lorentzian peak profile and subtracted from the $LaNiO_3$ and $LaNiO_2$ XAS to correct for the overlap between the tail of the La M_4-line and the Ni L_3-edge. The resulting spectra are shown in Fig. 2.

Theory calculations. For the oxygen PDOS shown in Fig. 1e–g and the electronic structure of $LaNiO_2$ shown in Fig. 3, LDA + U calculations were performed using the GGA method and the simplified version from Cococcioni and de Gironcoli[33], as implemented in QUANTUM ESPRESSO[34]. We find that an antiferromagnetic solution, with wavevector (π,π,π), leads to the lowest energy, with a two-Ni bct unit cell and corresponding Brillouin zone.

The Ni L_3-edge RIXS calculations (Fig. 2) were performed using an exact diagonalization technique[35,36], which accounts for the full overlap of the many-body wavefunctions. The microscopic Hamiltonian used for these calculations includes both material-specific on-site energies and hybridizations as encoded in a Wannier downfolding of the band structure[29] and the full set of Coulomb interactions as expressed in terms of Slater integrals. The relevant parameters used for Wannier downfolding paramagnetic $LaNiO_2$ (a one-Ni tetragonal unit cell), as shown in Supplementary Table 1, were obtained from Wannier90[37] for 12-orbital (O $p_x/p_y/p_z$, Ni $d_{z^2}/d_{x^2-y^2}/d_{xy}/d_{xz}/d_{yz}$, La d_{z^2}). The Slater integrals for Ni 3d in the $LaNiO_2$ calculations were $F^0=0.5719$ eV, $F^2=11.142$ eV and $F^4=6.874$ eV. The Slater integrals for Ni 3d–2p interactions were $F^0{}_{p,d}=0.148$ eV, $F^2{}_{p,d}=6.667$ eV, $G^1{}_{p,d}=4.922$ eV and $G^3{}_{p,d}=2.796$ eV. The values of F^2, F^4, $F^2{}_{p,d}$, $G^1{}_{p,d}$ and $G^3{}_{p,d}$ are taken from ref. [29]. We take 0.7 as a screening factor for the non-monopole terms. A core-level spin–orbit coupling of 12.5 eV was used for the Ni 2p core electrons. The resulting weight of the Ni wavefunction is shown in Supplementary Table 2.

The two-orbital, low-energy model for the physics of $LaNiO_2$ is shown in Fig. 4. This model, obtained once again by Wannier downfolding the DFT paramagnetic solution for $LaNiO_2$ in the one-Ni tetragonal unit cell (the same method as that used to obtain the non-interacting part of the Hamiltonian for the $LaNiO_2$ RIXS calculation, but only for the two bands that cross E_F), yields the independent hopping parameters listed in Supplementary Table 3, cut off for absolute values smaller than 0.008 eV. The two Wannier orbitals are shown in Fig. 4b: (1) a very extended orbital centred on La with $d_{3z^2-r^2}$ character, which makes up the majority character of the 3D band and (2) a more localized orbital, centred on Ni and primarily confined to the NiO_2 plane, with $d_{x^2-y^2}$ character, which makes up the majority character of the quasi-2D band. Note that this paramagnetic solution in the tetragonal Brillouin zone has one large quasi-2D hole-like Fermi surface from the Ni-centred orbital and two smaller 3D electron-like Fermi surfaces centred at the Γ- and A-points from the La-centred orbital. The low-energy, antiferromagnetic band structure from LDA + U (Fig. 3) would result from a (π,π,π) band-folding of the La-centred band, which moves the A-point to the Γ-point, formation of upper and lower Hubbard Ni-centred bands, gapping-out of the large hole Fermi surface, and a shift in chemical potential to compensate for the loss of carriers, which leaves a single electron pocket at the Γ-point.

The non-interacting bands of the effective low-energy model can be written in tight-binding form as

$$\begin{aligned}
\varepsilon^{\mathrm{R}}_{\mathrm{k}} = \quad & \varepsilon^{\mathrm{R}}_0 + 2\,\mathrm{t}^{\mathrm{R}}_{[0,0,1]}\cos(\mathrm{k_z}) + 2\,\mathrm{t}^{\mathrm{R}}_{[0,0,2]}\cos(2\,\mathrm{k_z}) + 2\,\mathrm{t}^{\mathrm{R}}_{[0,0,3]}\cos(3\,\mathrm{k_z})\\
& +2\,\mathrm{t}^{\mathrm{R}}_{[1,0,0]}\,[\cos(\mathrm{k_x})+\cos(\mathrm{k_y})]\\
& +4\,\mathrm{t}^{\mathrm{R}}_{[1,0,1]}\,[\cos(\mathrm{k_x})+\cos(\mathrm{k_y})]\cos(\mathrm{k_z})\\
& +4\,\mathrm{t}^{\mathrm{R}}_{[1,0,2]}\,[\cos(\mathrm{k_x})+\cos(\mathrm{k_y})]\cos(2\,\mathrm{k_z})\\
& +4\,\mathrm{t}^{\mathrm{R}}_{[1,1,0]}\,\cos(\mathrm{k_x})\,\cos(\mathrm{k_y})\\
& +8\,\mathrm{t}^{\mathrm{R}}_{[1,1,1]}\,\cos(\mathrm{k_x})\,\cos(\mathrm{k_y})\cos(\mathrm{k_z})\\
& +8\,\mathrm{t}^{\mathrm{R}}_{[1,1,2]}\,\cos(\mathrm{k_x})\,\cos(\mathrm{k_y})\cos(2\,\mathrm{k_z})\\
& +8\,\mathrm{t}^{\mathrm{R}}_{[1,1,3]}\,\cos(\mathrm{k_x})\,\cos(\mathrm{k_y})\cos(3\,\mathrm{k_z})\\
& +4\,\mathrm{t}^{\mathrm{R}}_{[2,0,1]}\,[\cos(2\,\mathrm{k_x})+\cos(2\,\mathrm{k_y})]\cos(\mathrm{k_z})\\
& +8\,\mathrm{t}^{\mathrm{R}}_{[2,1,1]}\,[\cos(2\,\mathrm{k_x})+\cos(\mathrm{k_y})\cos(\mathrm{k_x})\cos(2\,\mathrm{k_y})]\cos(\mathrm{k_z})
\end{aligned}$$

$$\begin{aligned}
\varepsilon^{\mathrm{Ni}}_{\mathrm{k}} = \quad & \varepsilon^{\mathrm{Ni}}_0 + 2\,\mathrm{t}^{\mathrm{Ni}}_{[1,0,0]}\,[\cos(\mathrm{k_x})+\cos(\mathrm{k_y})]\\
& +4\,\mathrm{t}^{\mathrm{Ni}}_{[1,1,0]}\,\cos(\mathrm{k_x})\,\cos(\mathrm{k_y})\\
& +2\,\mathrm{t}^{\mathrm{Ni}}_{[2,0,0]}\,[\cos(2\,\mathrm{k_x})+\cos(2\,\mathrm{k_y})]\\
& +2\,\mathrm{t}^{\mathrm{Ni}}_{[0,0,1]}\,\cos(\mathrm{k_z})\\
& +8\,\mathrm{t}^{\mathrm{Ni}}_{[1,1,1]}\,\cos(\mathrm{k_x})\,\cos(\mathrm{k_y})\cos(\mathrm{k_z})
\end{aligned}$$

where the appropriate matrix elements are provided in Supplementary Table 3.

Data availability

Raw data are shown in Figs. 1a–d and 2a–e, Extended Data Fig. 1 and Extended Data Fig. 2. The data that support the plots within this paper and other findings of this study are available from the corresponding authors upon reasonable request.

Code availability

QUANTUM ESPRESSO and Wannier90 are freely available at https://www.quantum-espresso.org and http://www.wannier.org, respectively. Access to RIXS exact diagonalization and Python analysis codes will be accommodated upon reasonable request to the corresponding authors.

References

30. Kawai, M. et al. Reversible changes of epitaxial thin films from perovskite $LaNiO_3$ to infinite-layer structure $LaNiO_2$. *Appl. Phys. Lett.* **94**, 082102 (2009).
31. Ikeda, A., Manabe, T. & Naito, M. Improved conductivity of infinite-layer $LaNiO_2$ thin films by metal organic decomposition. *Phys. C* **495**, 134–140 (2013).
32. Strocov, V. N. et al. High-resolution soft X-ray beamline ADRESS at the Swiss Light Source for resonant inelastic X-ray scattering and angle-resolved photoelectron spectroscopies. *J. Synchrotron Radiat.* **17**, 631–643 (2010).
33. Cococcioni, M. & de Gironcoli, S. Linear response approach to the calculation of the effective interaction parameters in the LDA + U method. *Phys. Rev. B* **71**, 035105 (2005).
34. Giannozzi, P. et al. QUANTUM ESPRESSO: a modular and open-source software project for quantum simulations of materials. *J. Phys. Condens. Matter* **21**, 395502 (2009).
35. Jia, C. J. et al. Persistent spin excitations in doped antiferromagnets revealed by resonant inelastic light scattering. *Nat. Commun.* **5**, 3314 (2014).
36. Jia, C., Wohlfeld, K., Wang, Y., Moritz, B. & Devereaux, T. P. Using RIXS to uncover elementary charge and spin excitations. *Phys. Rev. X* **6**, 021020 (2016).
37. Mostofi, A. A. et al. An updated version of Wannier90: a tool for obtaining maximally-localised Wannier functions. *Comput. Phys. Commun.* **185**, 2309–2310 (2014).

Acknowledgements

We thank G.A. Sawatzky and E. Benckiser for discussions. This work is supported by the US Department of Energy (DOE), Office of Science, Basic Energy Sciences, Materials Sciences and Engineering Division, under contract no. DE-AC02-76SF00515. X.F. and D.L. acknowledge partial support from the Gordon and Betty Moore Foundation's EPiQS Initiative through grant no. GBMF4415. Part of the synchrotron experiments were performed at the ADRESS beamline of the Swiss Light Source (SLS) at the Paul Scherrer Institut (PSI). The work at PSI is supported by the Swiss National Science Foundation through the NCCR MARVEL (research grant no. 51NF40_141828) and the Sinergia network Mott Physics Beyond the Heisenberg Model—MPBH (research grant no. CRSII2_160765/1). Part of the research was conducted at the Advanced Light Source (ALS), which is a DOE Office of Science User Facility, under contract no. DE-AC02-05CH11231. We acknowledge preliminary XAS characterization at BL13-3, SSRL by J.S. Lee in the early stage of the project.

Author contributions

W.S.L., M.H. and H.Y. Hwang conceived the experiment. M.H., H.L., E.P., Y.T., T.S. and W.S.L. conducted the experiment at SLS. H.L., W.S.L., Z.H. and Y.-D.C. conducted the experiment at ALS. H.L., W.S.L., A.N. and K.J.Z. conducted XAS measurement at Diamond Light Source. M.R., W.S.L., H.Y. Huang and D.J.H. conducted XAS measurements at NSRRC. J.S.L. contributed to XAS characterization of samples at an early stage of the work. M.H., H.L. and W.S.L. analysed the data. C.J.J., B.M., J.Z. and T.P.D. performed the theoretical calculations. D.L., X.F., Y.H., M.O. and H.Y. Hwang synthesized and characterized the nickelate samples using transport and XRD. M.H., Z.X.S. and W.S.L. prepared and aligned samples for X-ray spectroscopy measurements. M.H., B.M., J.Z. and W.S.L. wrote the manuscript with input from all authors.

Competing interests

The authors declare no competing interests.

Additional information

Extended data is available for this paper at https://doi.org/10.1038/s41563-019-0585-z.

Supplementary information is available for this paper at https://doi.org/10.1038/s41563-019-0585-z.

Correspondence and requests for materials should be addressed to C.J.J. or W.S.L.

Reprints and permissions information is available at www.nature.com/reprints.

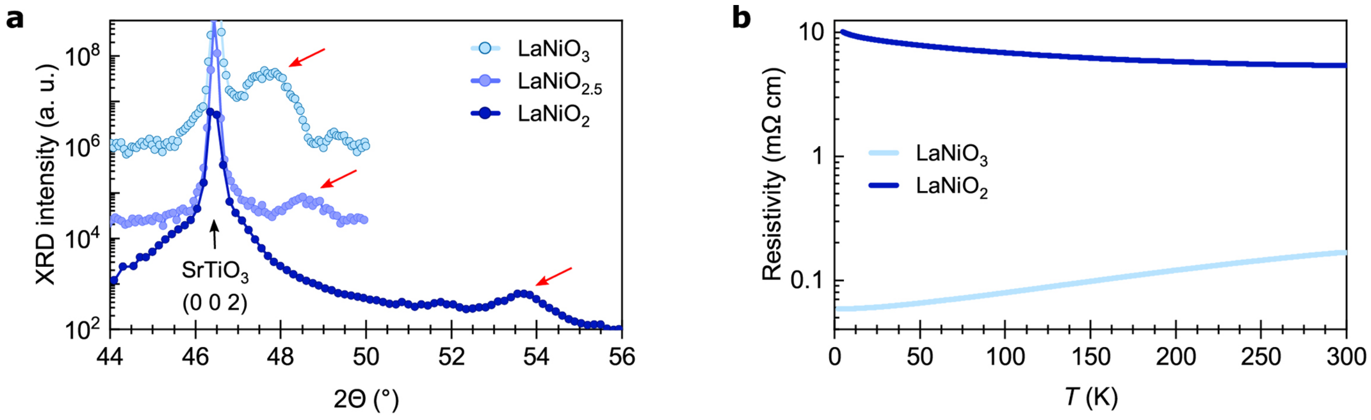

Extended Data Fig. 1 | XRD characterization and electrical transport measurements. **a**, XRD pattern of the $LaNiO_3$, $LaNiO_{2.5}$, and $LaNiO_2$ films grown on $SrTiO_3$ (001) substrates, measured with Cu Kα radiation. The red arrows indicate the nickelate film peaks and the black arrow the (002) $SrTiO_3$ substrate peak. The film peak shifts to higher 2θ values as a function of apical oxygen reduction. The curves are offset in vertical direction for clarity. **b**, Resistivity vs. temperature of the $LaNiO_3$ and $LaNiO_2$ film.

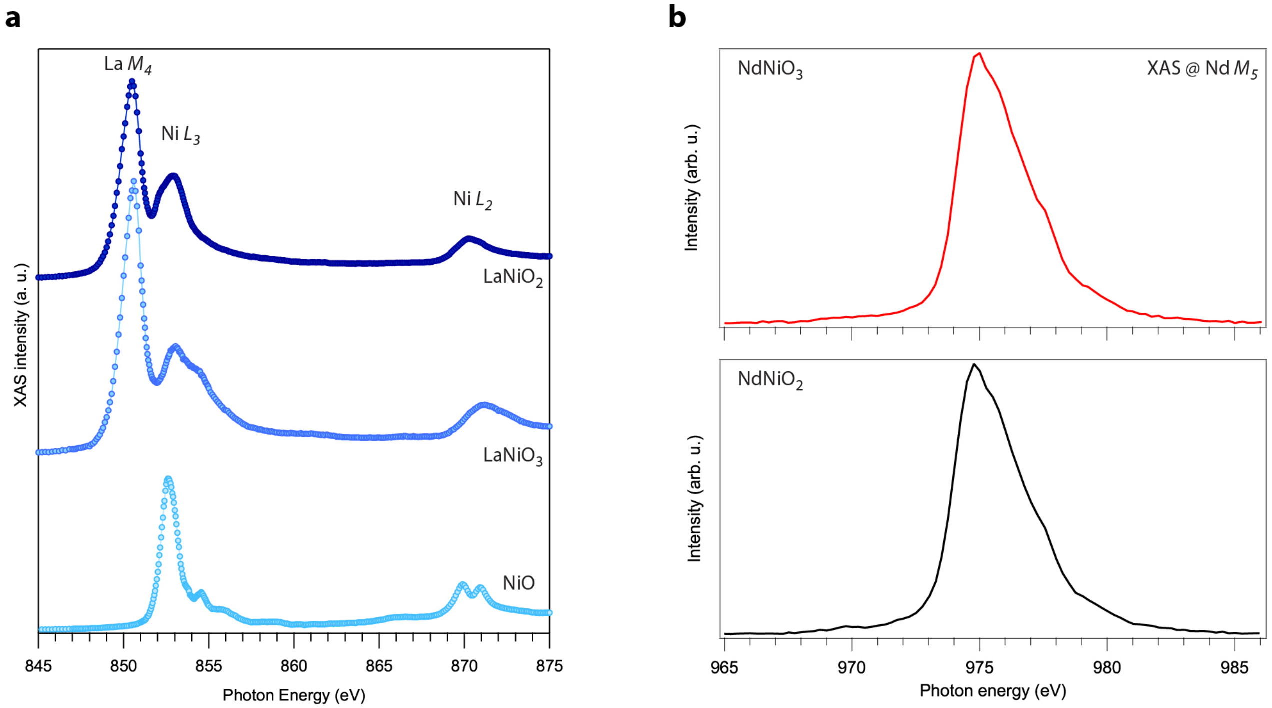

Extended Data Fig. 2 | Ni L-edge, La M_4-edge and Nd M_5-edge x-ray absorption spectra (XAS). a, XAS of $LaNiO_3$ and $LaNiO_2$ across the Ni $L_{3,2}$-edge before subtraction of the La M_4 absorption peak. The XAS of NiO powder is also shown. Spectra are offset in vertical direction for clarity. **b**, XAS of $NdNiO_3$ and $NdNiO_2$ across the Nd M_5-edge. The XAS were taken using total fluorescence yield. The XAS spectra across the rare-earth *M*-edges of the La- and Nd-based infinite-layer nickelates are essentially identical to those of their perovskite counterparts ($LaNiO_3$ and $NdNiO_3$). This implies a similar configuration of *4f* states for both types of nickelates and that the 4*f* states of La^{3+} and Nd^{3+} do not hybridize in any significant way with the Ni 3*d* states.

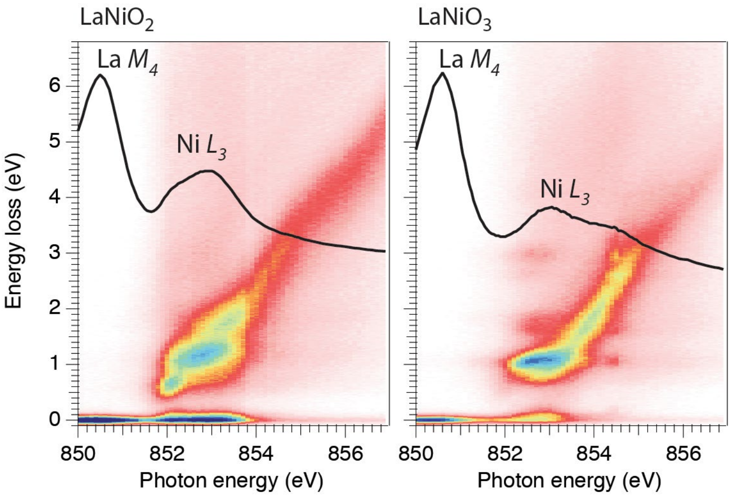

Extended Data Fig. 3 | RIXS maps across the La *M*$_4$-edge. RIXS maps for (left) LaNiO$_2$ and (right) LaNiO$_3$ with incident photon energies including the La *M*$_4$ edge. No orbital excitations exist in the inelastic channel of the RIXS spectra. This is consistent with a nominally empty 4*f* shell of the La^{3+} ion, implying that the 4*f* states are far from near-E_F states and not hybridized with the Ni 3*d* states.